



Low concentration nitric acid facilitate rapid electron–hole separation in vacancy-rich bismuth oxyiodide for photo-thermo-synergistic oxidation of formaldehyde



Yongchao Huang, Hanxi Hu, Shuxian Wang, Muhammad-Sadeeq Balogun, Hongbing Ji*, Yexiang Tong*

MOE of the Key Laboratory of Bioinorganic and Synthetic Chemistry, KLGHEI of Environment and Energy Chemistry, Chemical Industry Research Institute, School of Chemistry, The Key Laboratory of Low-carbon Chemistry & Energy Conservation of Guangdong Province, Sun Yat-sen University, Guangzhou 510275, China

ARTICLE INFO

Article history:

Received 16 February 2017

Received in revised form 18 June 2017

Accepted 10 July 2017

Available online 11 July 2017

Keywords:

Defects

Photocatalysis

Bismuth oxyhalide

Formaldehyde oxidation

Oxygen species

ABSTRACT

Searching for simple and effective methods for large-scale production of defective catalysts is of key importance, but remains a big challenge. Herein, we report a simple, scalable and effective method to produce defects in photocatalysts, which is significant for industrial application. Surprisingly, the defects on the photo-thermo-catalysts could not only availably decrease the recombination of photoelectrons and holes, but also increase the production of reactive oxygen species, which demonstrated a superior improvement in photo-thermo-catalytic activity coupled with ultrastable stability. These findings feature the fundamental role of surface defects structure on producing more oxygen reactive species and may create advance avenues for the rational design of extremely efficient photo-thermo-catalysts via surface engineering.

© 2017 Elsevier B.V. All rights reserved.

1. Introduction

Formaldehyde (HCHO) has been acknowledged as an indoor pollution, which may cause adverse effects on human health and are a main culprit for sick building syndrome [1]. Photocatalysis has been considered as a promising method to substantially solve this global environmental crisis [2–8]. Up to now, the photocatalytic activity is still far below the requirements of practical applications, which is restricted by the inactive charge-carrier separation in photocatalysts under the visible light irradiation [9–13]. Therefore, to enhance the photocatalytic efficiency of pollution degradation, the photoexcited electrons and holes should be consumed as far as possible during the photocatalytic process.

In principle, the photoelectrons are produced after the light irradiated the semiconductors. As some of them will recombine with the holes immediately, part of them will migrate to the surface of semiconductors and transfer the molecular oxygen to oxygen species, especially those physically adsorbed molecular oxygen on

the coordinative saturated oxide surface ($O_2 + e^- \rightarrow O_2^{\bullet-}$) [14–16]. These reactive oxygen species could efficiently oxidize the substrate molecules located at the neighboring sites [17]. So, the question is: (i) will increasing reactive oxygen species production in photocatalysis promote the photocatalytic activity of degradation pollution? And (ii) If possible, how can we increase the reactive oxygen species? Most recently, we had demonstrated that oxygen vacancies could effectively separate the photoexcited electrons and holes and then improve the photocatalytic performance [18–20]. Naturally, we were curious whether photoexcited electrons could migrate to the catalysts surface to produce reactive oxygen species with the help of oxygen vacancies. If this method is feasible, we only need to generate more reactive oxygen species while simultaneously improving the photocatalytic activity. In addition, the photoelectrons will move quickly as the temperature increases. Therefore, increasing the temperature during the reaction will enhance the separation of photoelectrons and holes, which may improve the photocatalytic performance? For our proof-of-concept demonstration, {001} bismuth oxyhalide (BiOI) nanosheets, due to its special structure and suitable band gaps (Scheme S1) [21,22], were employed as a model photocatalyst. However, the methods to produce defective bismuth oxyhalides are restricted by the dangerousness, high costs and difficulty in scaling-up [18–20]. For

* Corresponding author.

E-mail addresses: jihb@mail.sysu.edu.cn (H. Ji), chedhx@mail.sysu.edu.cn (Y. Tong).

examples, Ye et al. prepared oxygen defective BiOI by UV light irradiation with Ar blowing at high temperature [23]. Our previous work also demonstrated that BiOI with oxygen vacancies can be obtained via electroreduction, but this way was complicated [18]. A simple method was used to prepare oxygen defective BiOI nanosheets with NaBH₄ reducing reagents. The limitation of this way was that much hydrogen was produced in the reducing process, which was very dangerous for applications [20]. Thus, searching for simple and effective methods for large-scale production of defective catalysts is of key importance, but remains a big challenge.

Herein, for the first time, we demonstrated a simple and effective method to introduce oxygen vacancies into the {001} BiOI nanosheets via modifying with low concentrated nitric acid. Specifically, this method is highly suitable for industrial application due to the ease for large-scale production and cost-effectiveness. Enabled by the surface vacancies, more electrons transfer the molecular oxygen to reactive oxygen species, which facilitates charges separation. Meantime, the increase reactive oxygen species speed up the rate of reaction. Interestingly, our catalyst could not only be beneficial for the formaldehyde oxidation under visible light, but also exhibit significant improvement for thermal oxidation of formaldehyde. As a result, the efficiency of photo-thermocatalytic degradation gas formaldehyde exhibits 6 folds superior enhancement compared to that of untreated BiOI nanosheets. More importantly, no obvious deactivation of the defective BiOI was observed after cyclic reaction. This work sheds light on the vital role of defects in increasing reactive oxygen species production in photocatalysis.

2. Experimental section

2.1. Preparation of BiOI and deficient BiOI nanosheets

The {001} BiOI nanosheets were prepared according to our previous literature [24]. Deficient BiOI nanosheets were prepared by using {001} BiOI nanosheets as the precursor. In a typical synthesis, 0.1 g {001} BiOI nanosheets was immersed into nitric acid with different quantities (5 mL, 8 mL, 10 mL) and then added 50 mL water, stirring for 30 min at room temperature. The synthesis of the deficient BiOI nanosheets can be seen in Video S1. Finally, the products were collected and washed with deionized water four times, drying at 60 °C overnight. The deficient BiOI were labeled as BiOI-5, BiOI-8 and BiOI-10, respectively.

2.2. Characterization

The crystal phase of all the samples were analyzed by Raman spectrometry (Reinshaw), powder X-ray diffraction (D8ADVANCE), FT-IR spectra (Nicolet Avatar 370 infrared spectrometer) and X-ray photoelectron spectroscopy (ESCALab250, Thermo VG). Scanning electron microscope (JSM-6330F) and transmission electron microscopy (JEM2010-HR, 200 kV) were used to ensure the morphologies of all the samples. The thick of photocatalysts was measured by SPM-9500J3 microscope. The specific surface area was calculated by the Brunauer-Emmett-Teller (BET) method (ASAP 2020 V3.03H). Electron spin resonance (ESR) spectroscopy was used to examine unpaired electrons in materials at 77 K with a xenon lamp as the visible light source. DMPO (5,5'-dimethyl-1-pyrroline-*N*-oxide) was employed as a spin-trap reagent to trap the active species of hydroxyl (•OH) and superoxide radicals (•O₂[−]). 50 μL (1 g L^{−1}) BiOI suspension and 50 μL of DMPO (25 g L^{−1}) were mixed in different solvents in line with the targeted radical. Water and DMSO were used for hydroxyl (•OH) and superoxide radicals (•O₂[−]) trapping, respectively. The optical properties of all the

samples were recorded by the UV–vis spectrophotometer (UV-2450), using BaSO₄ as the reflectance standard. Photoluminescence spectra (360 nm excitation) and time-resolved PL spectra (255 nm excitation) were recorded by a FLSP920 multifunction steady state and transient state fluorescence spectrometer. The electrochemical measurements of all the samples were performed with a standard three-electrode, which has been reported in our previous literature [24].

2.3. Photocatalytic activity tests

Photocatalytic performances of all samples were evaluated by the removal of HCHO (500 ppm). The catalysts (0.05 g) were put in the reactor, as shown in Scheme S2. Gaseous HCHO was generated by passing a purified air flow (N₂/O₂ = 4100 mL min^{−1}) over HCHO solution in an incubator kept at 0 °C. The reaction flask was put in a cooling water system to keep the reaction at room temperature. Prior to irradiation, the catalyst was magnetically stirred in the dark for 120 min to establish absorption–desorption equilibrium. A Xe lamp (300 W) was used as the visible light source with a UV light cutoff filter (420 nm). A gas chromatograph (Agilent 7890A) with a TCD detector and a Porapak-Q column was used to analyze the production of CO₂. The HCHO conversion was calculated by the follows:

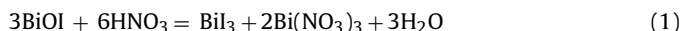
$$\text{HCHO conversion}(\%) = [\text{CO}_2]/[\text{HCHO}]_{\text{total}} \times 100$$

[CO₂] and [HCHO]_{total} in the formula are the CO₂ concentration in the products and the total HCHO concentration in the reactor, respectively. After the experiment, N₂ was bubbled into the photoreactor at a flow rate of 100 mL min^{−1} to eliminate the HCHO in the photoreactor. Gaseous HCHO was generated again to evaluate the cycling photocatalytic performance.

3. Results and discussion

3.1. Synthesis and characterization of all the catalysts

The {001} BiOI nanosheets were prepared according to our previous literature [24]. The defective BiOI nanosheets were obtained by modifying the BiOI nanosheets with nitric acid at room temperature, which is a simple and effective method, as shown in Fig. 1a. The pristine BiOI nanosheets turn from red to black after injecting 2 mL HNO₃ solution, which was confirmed to be BiI₃ by X-ray diffraction patterns (XRD) and Raman spectroscopy (Eq. (1)) [25].



The XRD of BiI₃ is shown in Fig. 1b, which can be indexed to the rhombohedral BiI₃ (PDF no:48-1795). Likewise the Raman spectrum shown in Fig. 1c confirms the BiI₃ with corresponding peaks at 84, 114 and 154 cm^{−1}, which are attributed to A_g, E_g and A_g mode, respectively [25]. By adding water into the BiI₃ solution, the defect-rich BiOI was formed with the solution turning red immediately (Eq. (2)).



The whole process in the preparation of the defective BiOI can be seen in Video S1, and in this change process, some defects are produced (Fig. S1). More importantly, the concentrations of defects could also be controlled by the content of HNO₃ concentration, labeling as BiOI-5, BiOI-8 and BiOI-10, respectively.

In order to prove that this is a feasible method to construct defect-rich BiOI nanosheets, we apply this simple and scalable method to another pristine BiOI (d-BiOI) photocatalyst, which was prepared differently from {001} BiOI nanosheets [18]. It is worthy

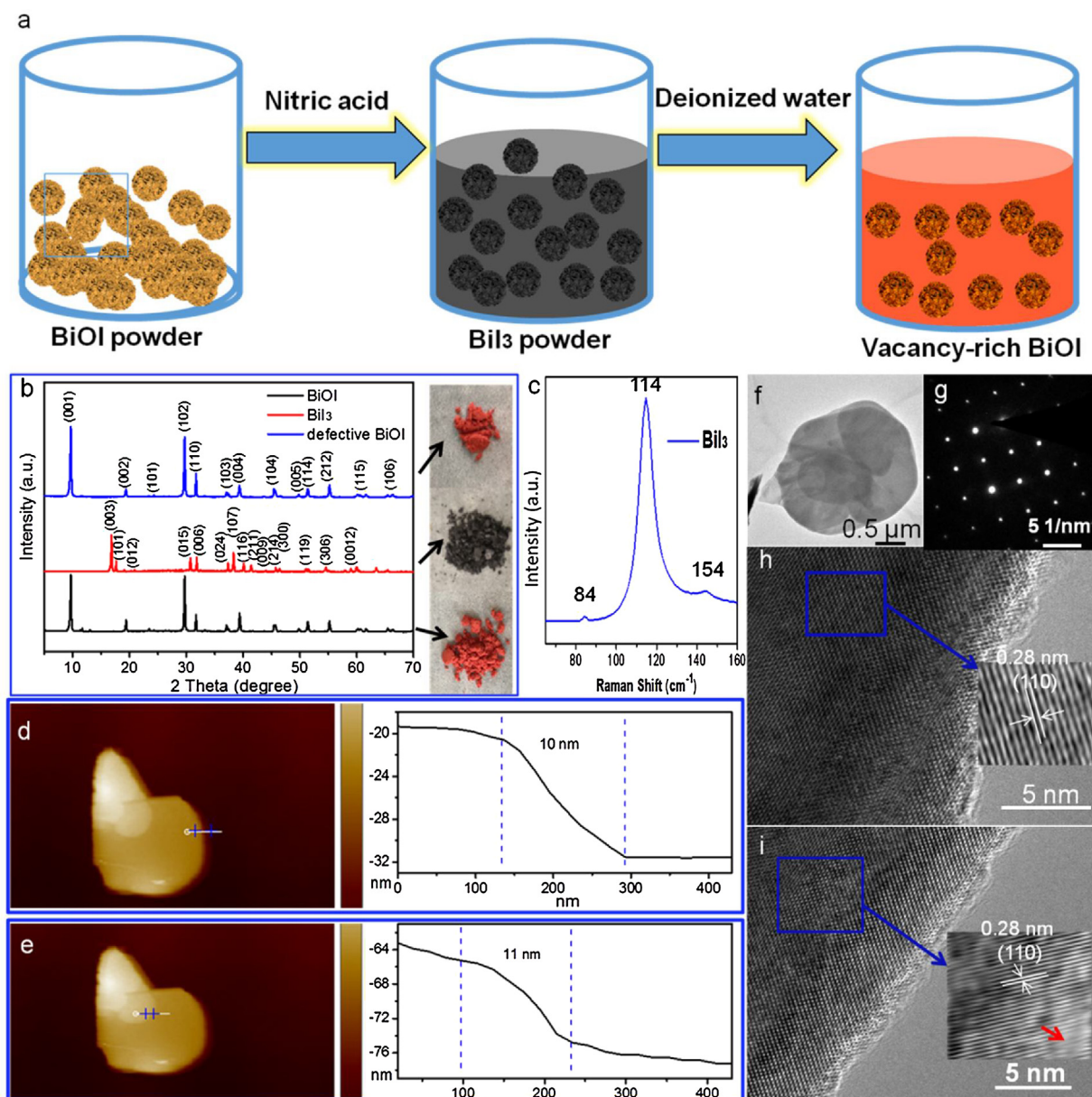


Fig. 1. (a) Schematic diagram illustrating the growth process of defective BiOI nanosheets. (b) XRD pattern and Photographs of BiOI, BiI₃ and defects rich BiOI nanosheets. (c) Raman pattern of BiI₃. (d) and (e) AFM images of BiOI-8 nanosheets. (f) BiOI nanosheets of low-resolution TEM image. (g) The selected-area electron diffraction of BiOI nanosheets. HRTEM images of (h) BiOI nanosheets and (i) BiOI-8 nanosheets.

of noting that similar phenomena for the preparation of defect-rich {001} BiOI was observed (Fig. S2). The defective BiOI was also obtained, suggesting that it is a simple, feasible, repeatable and effective method to introduce defects into BiOI photocatalysts.

Fig. 2 shows the structure of pristine BiOI and defective BiOI nanosheets, which were then characterized by XRD, Raman spectroscopy, FT-IR and Brunauer–Emmett–Teller (BET) specific surface areas. The XRD patterns of all the BiOI-based catalysts could be indexed to the tetragonal BiOI (PCPDF no.: 10-0445). The {001}, {002}, {003} and {004} peaks are stronger and sharper, while {110} diffraction peaks is relatively weak, suggesting BiOI gives priority to grow along the c axis ([001] orientations) perpendicular to the nanosheets [26]. The {001} surface of BiOI is a close-packed structure, exposing high-density O atoms. The Raman peaks at 85 cm⁻¹ and 147 cm⁻¹ are attributed to the Bi–I vibration of BiOI (Fig. 2b). In Fig. 2c, for pure BiOI, a peak at 489 cm⁻¹ in the spectrum corresponding to symmetrical A_{2u}-type vibration of the Bi–O bond

was observed, and is consistent with the published results [18]. The absorption at 745 cm⁻¹ was assigned to the asymmetrical stretching vibration of Bi–O bond. However, after introducing vacancy into BiOI-8, the peak at 772 cm⁻¹ change to 745 cm⁻¹, which may be the vacancy affect the asymmetrical stretching vibration of Bi–O bond. In addition, the presence of the sharp and strong absorption at 1621 cm⁻¹ and a broad peak at 3430 cm⁻¹ were ascribed to the δ(O–H) bending vibration and ν(O–H) stretching respectively due to the adsorption of free water molecules on the photocatalyst surface. The BET specific surface area of pristine BiOI and defective BiOI nanosheets are about 3.04 m²/g, suggesting that the structure and morphology has no changed. As shown in Fig. S3, the nanosheets with various edge lengths and same thickness display {001} faces on flat surfaces. The BiOI-8 nanosheets have a thickness of about 10 nm, indicating its ultrathin nature, as demonstrated by Atomic force microscopy (AFM) (Fig. 1d and e). To go deep into the morphology of the BiOI and BiOI-8 nanosheets, transmission electron

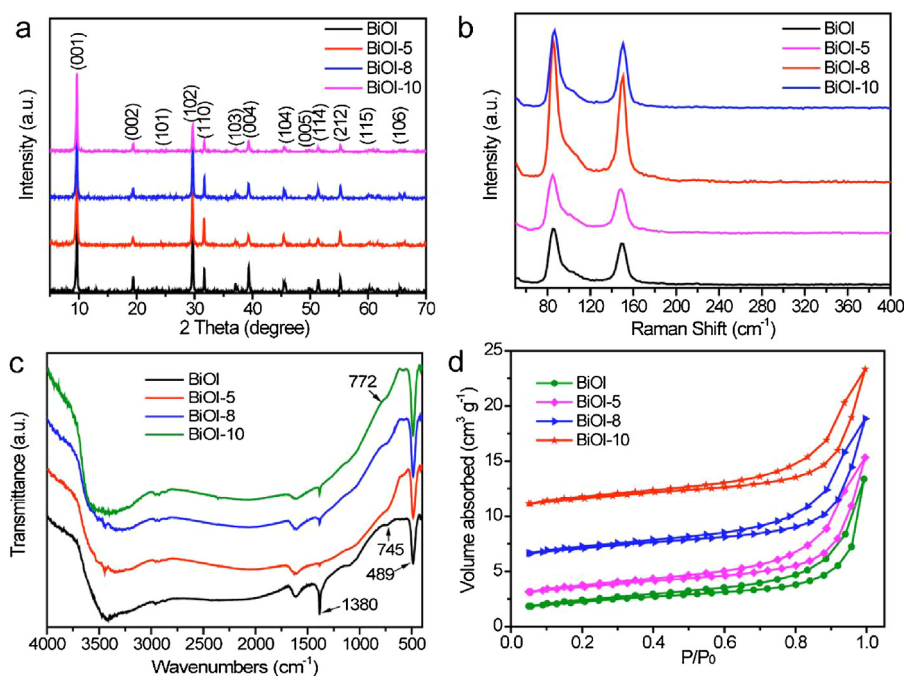


Fig. 2. (a) XRD patterns, (b) Raman spectra, (c) FT-IR spectra and (d) BET specific surface area analysis of all the samples.

microscopy was performed. The low-resolution TEM image (Fig. 1f) and selected-area electron diffraction analysis (Fig. 1g) of BiOI reveal the single crystal nanosheets. The BiOI nanocrystals were highly crystallized, as seen from the high-resolution TEM (HRTEM) (Fig. 1h). The well resolved lattice features could be seen and the lattice fringes with an interplanar spacing of 0.28 nm are confirmed to the {110} planes of tetragonal BiOI (PCPDF no.: 10-0445). After treatment with nitric acid, the morphology of BiOI-8 was maintained (Fig. S4), however, the lattice fringes became disordered, which can be seen in Fig. 1i, suggesting the existence of defects [27,28]. These defect structures can act as catalytically active sites for photocatalysis.

3.2. Characterization of vacancies on BiOI nanosheets

To directly identify the oxygen vacancies, a set of advanced techniques were carried out to describe the deficient BiOI nanosheets, using the untreated BiOI nanosheets as a reference. Firstly, electron spin resonance (ESR) spectroscopy was used to examine the unpaired electrons in materials and verify the existence of vacancies [23,28–30]. The deficient BiOI nanosheets demonstrated the symmetrical ESR signals at $g=2.002$, suggesting the electron trapping at defects (Fig. 3a). This phenomenon could be observed in other semiconductors, such as TiO₂ [28,30], BiOCl [23] and ZnO [31]. The BiOI-10 had a strongest signal, maintaining the highest density oxygen vacancy. But BiOI-8 had the highest performance in degradation of HCHO. It was because too much oxygen vacancy could act as the recombination center, decreasing charge transfer to catalyst surface. Further auxiliary evidence of the existence of defects was provided by the Thermogravimetry analysis (TGA), in that the vacancies can be re-filled with oxygen as shown in Fig. 3b. According to Xie's group, it had been demonstrated that oxygen vacancy could enhance the absorption of H₂O due to the low-coordination which suggest slower weight loss defect-rich samples [32]. The TGA measurement of the BiOI consist of two reaction stages (below and after 230 °C). Below 230 °C, the physically absorbed water from BiOI surface were lost [32]. Beyond 230 °C, the BiOI gradually oxidized to Bi₂O₃. After the physically absorbed surface water of the

entire BiOI samples had been lost, the deficient BiOI catalysts utilized its vacant sites to react with the O₂ gas up to 450 °C before the weight loss process, unlike the bare BiOI sample that exhibited drastic weight loss immediately after 230 °C. Although, defects were formed in deficient BiOI nanosheets, however, X-ray photoelectron spectroscopy (XPS) indicate that the valence state of Bi did not changed as shown in Fig. S5. This is different from our previous studies, suggesting the defects were not Bi²⁺ vacancies. It is well known that vacancies could provide coordinatively unsaturated sites for oxygen species chemisorption, which can be characterized by the O 1s of XPS. Fig. 3c and Fig. S6 show the O 1s spectra of catalysts, which were also deconvoluted. The peaks at 529.5 eV can be indexed to the lattice oxygen, which could be observed in oxide semiconductors. Notably, addition peaks at 537.1 eV and 532.5 eV appear in the spectrum of deficient BiOI nanosheets, arising from the oxygen species chemisorbed and physically absorbed water at oxygen vacant sites, respectively [32]. This is in line with the TGA results. Noting that the new peaks at 621.5 eV appear in the spectrum of deficient BiOI nanosheets, suggesting that the vacancies may come from the iodide defects (Fig. 3d). Combining the results of ESR and TGA above, we undisputedly conclude that defects were successfully generated in the defective BiOI nanosheets, offering the prerequisite for studying the relationship between reactive oxygen species and vacancies in photocatalysis (Fig. 3e).

Defects could affect the charge carrier dynamics of photocatalysts, which promote the charge transfer to the surface of semiconductors [33,34]. Fig. 4a shows the transient photocurrent response of BiOI and deficient BiOI nanosheets at a bias of 0.6 V (Vs Ag/AgCl). The photocurrent density of deficient BiOI nanosheets displayed higher than that of pure BiOI nanosheets and BiOI-10 showed lower density than that of BiOI-8. This is probably due to excessive defects will become the recombination centers of photoelectrons and holes, decreasing the charge transfer to surface [33]. Moreover, the electrochemical impedance spectroscopy (EIS) Nyquist plots also revealed that BiOI-8 nanosheets has the fastest interfacial charge transfer characteristics under dark or visible light irradiation, which owned the smallest radius (Fig. 4b). Furthermore, the distinguished photoluminescence spectra suggested that

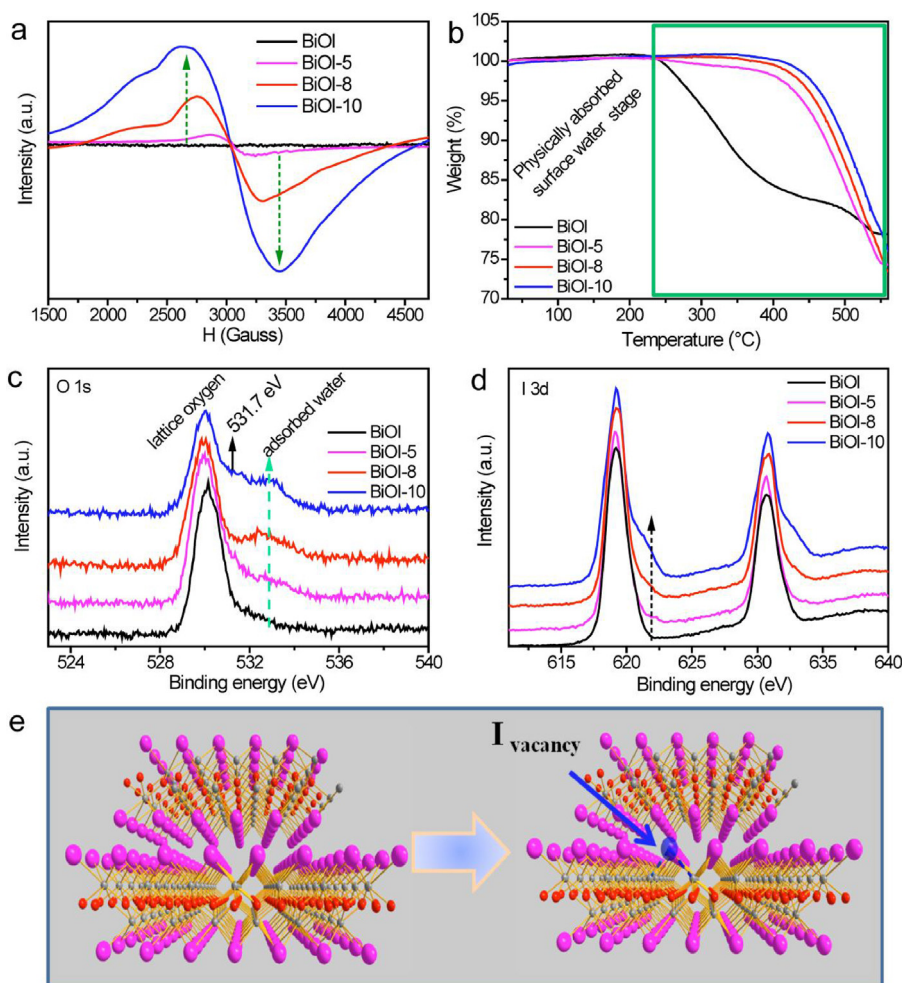


Fig. 3. (a) ESR spectra of BiOI and deficient BiOI nanosheets. (b) TG spectra of BiOI and deficient BiOI nanosheets. (c) High-resolution O 1s XPS spectra and (d) high-resolution I 3d XPS spectra of BiOI and deficient BiOI nanosheets.

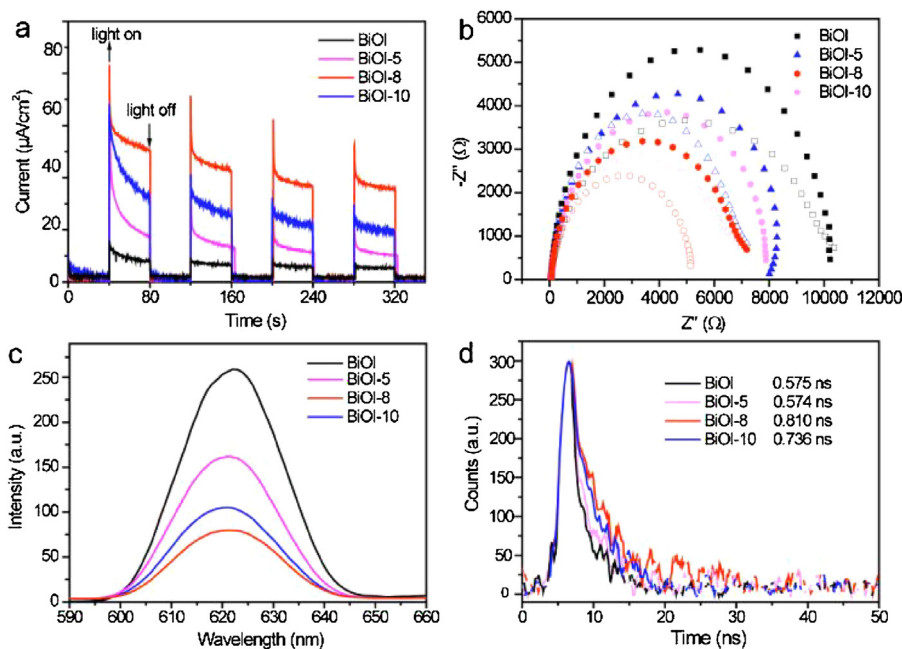


Fig. 4. (a) Transient photocurrent response, (b) electrochemical impedance spectroscopy in dark and under visible light irradiation, (c) photoluminescence spectra with 400 nm excited wavelength and (d) Time-resolved photoluminescence spectra of BiOI and deficient BiOI nanosheets.

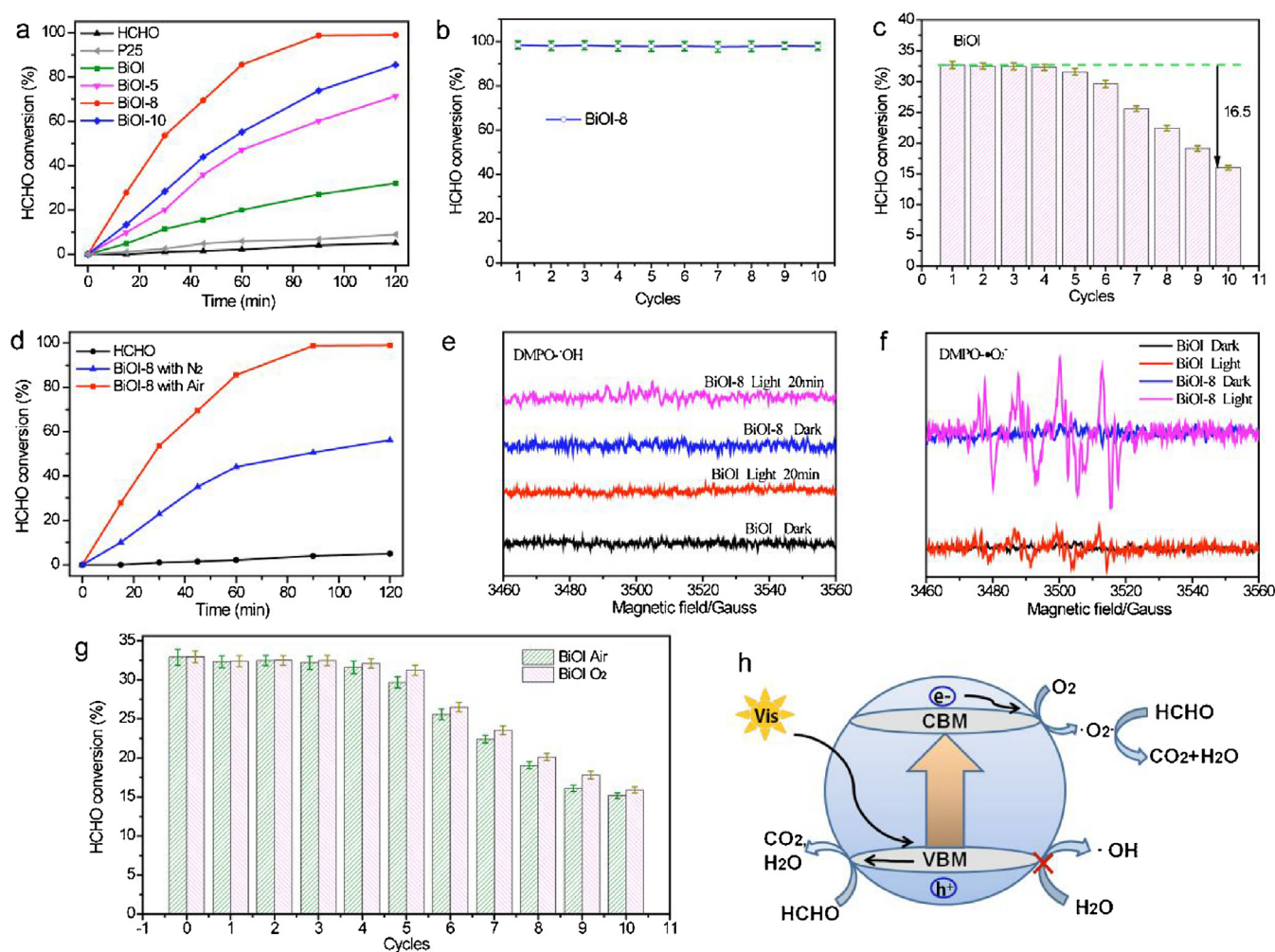


Fig. 5. (a) Photocatalytic performance of all the samples with the irradiation of visible light. (b) Cycling measurements for the BiOI-8 nanosheets. (c) Cycling measurements for the BiOI nanosheets. (d) Photocatalytic activity of BiOI-8 nanosheets under air and N₂ atmosphere. ESR measurements of (e) DMPO-•OH and (f) DMPO-•O₂⁻ for BiOI and BiOI-8 nanosheets with and without visible light irradiation (λ ≥ 420 nm). (g) Cycling measurements for BiOI nanosheets under air and O₂ atmosphere. (h) Photocatalytic mechanism scheme of deficient BiOI sample.

deficient BiOI nanosheets possess better electron-hole separation capacity (Fig. 4c). The lifetime of charge carriers is recognized as a vital parameter to the efficacy of the transfer and separation of photoexcited carriers in the photocatalytic system [33,34]. Therefore, the lifetime of charge carriers of BiOI and deficient BiOI nanosheets were also carried out by time-resolved photoluminescence (Fig. 4d). The lifetime of deficient BiOI-8 nanosheets was estimated to be almost 0.810 ns, which was 1.4 times longer than that of BiOI nanosheets observed at 0.575 ns, suggesting that defects can increase the separation efficiency of photoinduced carriers. Coupled with EIS plots, such behaviors revealed the BiOI nanosheets have the good electrical conductivity. Fig. S7 shows the Mott-Schottky plots of all samples under the dark. BiOI-8 nanosheets have high carrier density, indicating that defects can commonly enhance the charge transfer. All the results above demonstrated that defects can superiorly separate the photoelectrons and holes, which was vital for photocatalysis.

3.3. Photo-thermo-catalytic activity of all catalysts

To shed light on the role at defects and certify the expectation that more reactive oxygen species were produced in photocatalytic process, the mineralization of gas volatile organic compounds with pristine BiOI and deficient BiOI nanosheets were carried

out under the irradiation of visible light (λ ≥ 420 nm) by a 300 W Xe lamp (Scheme S2). Formaldehyde, one of the volatile organic compounds, due to its tremendous carcinogenicity, has been considered as a preferred hazardous substance for photocatalytic air purification [35,36]. As depicted in Fig. 5a, the self-degradation of HCHO can be ignored under our testing. Significantly, being lighted for 90 min, the photocatalytic performance of BiOI-8 nanosheets is approximately 100%, which is 5 times higher than that of pristine BiOI nanosheets, suggesting the improved photocatalytic performance of BiOI-8 nanosheets. The catalytic performance of the BiOI-8 is superior to those of other photocatalysts (Table S1), such as Fe₂O₃/TiO₂ (T_{82.4%} = 180 min) [37], TiO₂ NTs (T_{100%} = 240 min) [38], MnOx modified Co₃O₄ (T_{85%} = 180 min) [39], Eu-CeO₂ (T_{90%} = 120 min) [40]. Notably, compared with BiOI-10 nanosheets, BiOI-8 nanosheets have the better performance, which can be attributed to too much defects that could decrease surface charge transfer to surface. Furthermore, BiOI-8 nanosheets display the excellent stability without any decays even after 10 consecutive cycles with accumulatively 20 h (Fig. 5b). Whereafter, the stability of pristine BiOI were also performed 10 consecutive cycles. Unexpectedly, the photocatalytic performance of BiOI nanosheets drops severely after 5 cycles and decreased to 18.5% after 10 cycles (Fig. 5c). The morphology and phase structure of BiOI and BiOI-8 nanosheets after 10 cycles reaction also reveal the

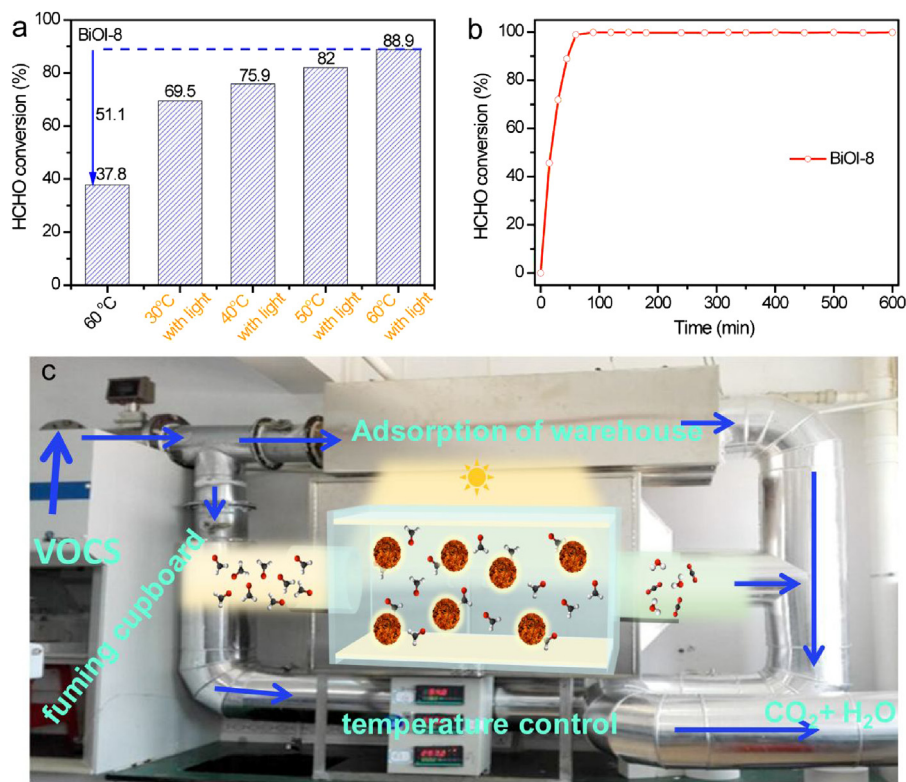


Fig. 6. (a) Photocatalytic degradation of HCHO at different temperature at 45 min. (b) Cycling measurements for the BiOI-8 nanosheets. (c) Photograph of large-scale photocatalytic devices.

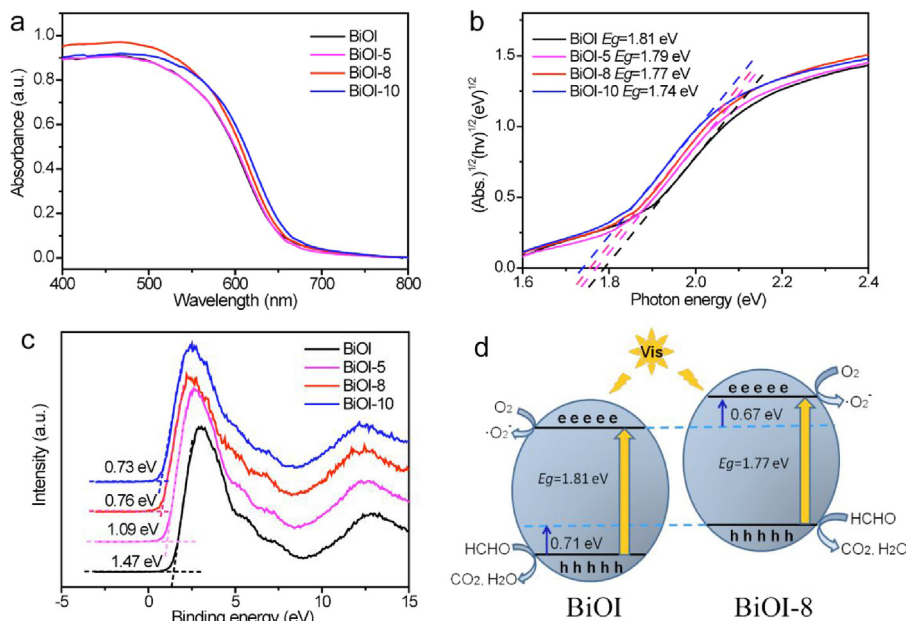


Fig. 7. (a) UV-vis absorption spectra of the BiOI nanosheets and defective BiOI nanosheets. (b) Optical band gaps regulate by UV-vis diffuse reflectance spectra. (c) Comparing the valence band of BiOI nanosheets and defective BiOI nanosheets. (d) Schematic band structure of BiOI nanosheets and defective BiOI-8 nanosheets.

stability (Fig. S8). These results demonstrated that defects could enhance the stability of HCHO oxidation. What aroused our interest is how the defects enhance the stability? Weon et al. observed severe deactivation of TiO₂ nanospheres for toluene degradation due to carbonaceous deposits on the catalysts surface, which can be detected by FT-IR analysis [41]. Motivated by Weon's work, we compared the FT-IR analysis of BiOI nanosheets before and after 10 cycles reaction and some functional groups were found, suggesting

carbonaceous intermediates deposits may be the main reason for the photocatalyst deactivation (Fig. S9). Defects could effectively enhance the charge migrating to the surface, so we proposed that more reactive oxygen species were produced during the photocatalytic process, thereby maintaining the catalytic performance of the defect-rich photocatalysts. Thus, the photocatalytic activity of BiOI-8 nanosheets was carried out in pure N₂ atmosphere, which is shown in Fig. 5d. Compared with the BiOI-8 nanosheets

in air, the performance under pure N₂ atmosphere is obviously reduced, suggesting O₂ plays a vital role in photocatalysis. Photoexcited electrons migrated to the catalysts surface to produce reactive oxygen species with the help of oxygen vacancies, which markedly increased the performance. To trace the vestige of O₂, we employed 5,5-dimethyl-1-pyrroline N-oxide (DMPO) in water and in methanol to examine the •OH and •O₂[−]. As shown in Fig. 5e, no signals of •OH were detected by pristine BiOI and deficient BiOI-8 nanosheets regardless in the dark or under the light irradiation. This reveals that there is no •OH produced in photocatalytic progress, meaning the reactive holes in their valence bands directly oxidized the HCHO [42]. The presence of water will affect the production of •OH radicals, accordingly to $\text{H}_2\text{O} + h\nu_{\text{VBM}} \rightarrow \bullet\text{OH} + \text{H}^+$. However, the VBM of BiOI can not oxidize H₂O. So the presence of water will not affect the production of •OH. The oxidizing capability of photogenerated holes was determined by the position of the VB maximum. Moreover, no •O₂[−] was generated by pristine BiOI or deficient BiOI nanosheets in the dark. As the light turns on, four ESR signals from •O₂[−] were observed, a nearly 1:1:1:1 quartet pattern (Fig. 5f). The signal intensity of BiOI-8 nanosheets is markedly higher than that of BiOI nanosheets, revealing that defects could effectively activate O₂ molecule into •O₂[−] species. This suggests that introducing vacancies into semiconductors will generate more reactive oxygen species while simultaneously improving the photocatalytic activity. If this is the case, the performance of BiOI nanosheets will not increase obviously under pure O₂ atmosphere. The deactivation of BiOI nanosheets slightly decreases under pure O₂ atmosphere (Fig. 5g), which is because O₂ acts as a reagent required for the mineralization of organic substances ($\text{R}^* + \text{O}_2 \rightarrow \text{CO}_2$). Upon decoding the photocatalytic reaction process, the mechanistic pathway is clarified in Fig. 5h. The photoelectrons migrate to the surface defects sites and activate the chemisorbed O₂ into •O₂[−], which plays the main role in photocatalytic performance. In the meantime, the photoexcited holes directly oxidize the HCHO into CO₂ and H₂O. In this way, the photoelectrons and holes are separately available under the visible light irradiation and the defects could constantly provide surface sites to increase more reactive oxygen species.

Vacancies may become mobile, which are more difficult to trap sites at increasing temperature. Thus, we studied the effect of increasing temperature (30–60 °C) coupling with irradiation of visible light on the mineralization of HCHO. Surprisingly, as shown in Fig. 6a, the catalytic performance of BiOI-8 nanosheets increased as the temperature rising under visible light. The catalytic activity of the BiOI-8 nanosheets at 60 °C is 20% higher than the one at ambient temperature. Such enhanced performance of the BiOI-8 nanosheets can be attributed to the synergistic effect from the free mobility of the electrons in the vacant sites during temperature increment. Hence, this phenomenon suggests our as-prepared BiOI-8 nanosheets is a “photo-thermo catalyst”. In order to identify that the enhanced degradation of HCHO at 60 °C was due to photo-thermo-catalysis, the catalytic activity without light was performed, and only low performance was observed. Fig. 6b shows the stability of photo-thermo BiOI-8. The photo-thermo-catalytic performance of BiOI-8 nanosheets was retained after 600 min, suggesting a wonderful stability. Note that the BiOI-8 nanosheets had been tested in industrial applications (Huizhou Research Institute of Sun Yat-Sen University, Huizhou, PR China). The process of photo-thermo-catalytic oxidation can be seen in Fig. 5c.

3.4. Reaction mechanism

It has been widely acknowledged that lattice defects greatly change the band structure of semiconductors, which strongly influence the absorption capability [18,42,43]. As shown in Fig. 7a, defective BiOI nanosheets display a slightly red-shift absorption

edge than that of pristine BiOI nanosheets, suggesting defective BiOI nanosheets could use more visible light. This is integrally essential for photocatalysts to generate the photoelectrons and holes under the light irradiation. As BiOX (X = Cl, Br, I) are known as indirect semiconductors, the band gap can be obtained from $a = A(h\nu - E_g)^2/h\nu$, where a is the absorption coefficient, A is the absorption constant for indirect transition [23,44]. The band gap (E_g) of the BiOI nanosheets is calculated to be 1.81 eV, which is a bit larger than those of the defective BiOI nanosheets (1.77–1.74 eV). Defects will change the surface atomic arrangement, exhibiting different electronic band structures [45]. XPS valence spectra was performed to measure the relative location of valence band maximum (VBM) for all the samples [46]. As shown in Fig. 7c, the valence band maximum of BiOI nanosheets is 1.47 eV, which is larger than that of defective BiOI nanosheets. According to the above results, the band structures of BiOI nanosheets and defective BiOI-8 nanosheets are illustrated schematically in Fig. 7d. Comparing to the pristine BiOI nanosheets, the VB width and elevated CB minimum of BiOI-8 nanosheets are enhanced, suggesting a much better consumption of photoexcited holes and a higher reduction ability to form reactive oxygen species for BiOI-8 nanosheets in the photocatalytic process [29,47]. In other word, this features of the energy band structure for defective BiOI nanosheets are constructive for separating the photoexcited electron-hole pairs, which may be the main reason for the production of more reactive oxygen species and improving the photocatalytic activity of the defective BiOI nanosheets.

4. Conclusions

In conclusion, we have demonstrated a simple and effective method to introduce oxygen vacancies into the {001} BiOI nanosheets via modified with low concentrated nitric acid for the first time, which is highly suitable for industrial application due to the ease for large-scale production and cost-effectiveness. The vacancy associated BiOI nanosheets as an outstanding platform to promote the photo-thermo-catalytic performance by increasing reactive oxygen species production. The vacancy elevated the valence-band maximum of BiOI nanosheets, ensuring more charge carriers transform into •O₂[−] in photo-thermo-catalysis. Furthermore, defective BiOI nanosheets could use more visible light than pristine BiOI nanosheets, which is significant for improving the photo-thermo-catalytic performance. As a result, the defective BiOI nanosheets demonstrated a superior improvement in photo-thermo-catalytic activity accompanied with wonderful stability. This work not only offers an appropriate plan for the construction of high-performance and stable photo-thermo-catalytic via vacancy associating, but also sheds light on the vital role of defects in increasing reactive oxygen species production in photo-thermo-catalysis.

Acknowledgments

This work was preliminarily supported by the National Science Fund for Distinguished Young Scholars (21425627), the Natural Science Foundation of China (21461162003 and 21476271), National Natural Science Foundation of China-SINOPEC Joint fund (U1663220) and Natural Science Foundation (2014KTSCX004, 2014A030308012 and S2013030013474) of Guangdong Province, Jiangsu Key Laboratory of Vehicle Emissions Control (OVEC019), Nanjing University and supported by “the Fundamental Research Funds for the Central Universities (17lgpy74)”.

Appendix A. Supplementary data

Supplementary data associated with this article can be found, in the online version, at <http://dx.doi.org/10.1016/j.apcatb.2017.07.028>.

References

- [1] S. Rong, P. Zhang, Y. Yang, L. Zhu, J. Wang, F. Liu, *ACS Catal.* 7 (2016) 1057–1067.
- [2] Y. Cui, Q. Ma, X. Deng, Q. Meng, X. Cheng, M. Xie, X. Li, Q. Cheng, H. Liu, *Appl. Catal. B Environ.* 206 (2017) 136–145.
- [3] K. Li, Y. Tang, Y. Xu, Y. Wang, Y. Huo, H. Li, J. Jia, *Appl. Catal. B Environ.* 140 (2013) 179–188.
- [4] X. Chen, Y. Li, X. Pan, D. Cortie, X. Huang, Z. Yi, *Nat. Commun.* 7 (2016) 12273.
- [5] A. Li, T. Wang, X. Chang, W. Cai, P. Zhang, J. Zhang, J. Gong, *Chem. Sci.* 7 (2015) 890–895.
- [6] L. Hao, S. Jian, Z. Ai, L. Zhang, *J. Am. Chem. Soc.* 137 (2015) 6393–6399.
- [7] D.J. Martin, G. Liu, S.J.A. Moniz, Y. Bi, A.M. Beale, J. Ye, J. Tang, *ChemInform* 44 (2015) 7808–7828.
- [8] B. Cao, G. Li, H. Li, *Appl. Catal. B Environ.* 194 (2016) 42–49.
- [9] A. Li, X. Chang, Z. Huang, C. Li, Y. Wei, L. Zhang, T. Wang, J. Gong, *Angew. Chem. Int. Ed.* 55 (2016) 13734–13738.
- [10] J. Jiang, K. Zhao, X. Xiao, L. Zhang, *ChemInform* 134 (2012) 4473–4476.
- [11] H. i. Kim, H. -n Kim, S. Weon, G.-h Moon, J.-H. Kim, W. Choi, *ACS Catal.* (2016) 8350–8360.
- [12] Y. Huo, X. Chen, J. Zhang, G. Pan, J. Jia, H. Li, *Appl. Catal. B Environ.* 148 (2014) 550–556.
- [13] J. Wang, W. Jiang, D. Liu, Z. Wei, Y. Zhu, *Appl. Catal. B Environ.* 176 (2015) 306–314.
- [14] H. Yin, X. Chen, R. Hou, H. Zhu, S. Li, Y. Huo, H. Li, *ACS Appl. Mater. Interfaces* 7 (2015) 20076–20082.
- [15] Y. Huo, R. Hou, X. Chen, H. Yin, Y. Gao, H. Li, *J. Mater. Chem. A* 3 (2015) 14801–14808.
- [16] Y. Zhu, L. Qiang, Y. Liu, W. Hua, Y. Zhu, *Appl. Catal. B Environ.* 187 (2016) 204–211.
- [17] Y. Liu, W. Yao, L. Di, R. Zong, Z. Mo, X. Ma, Y. Zhu, *Appl. Catal. B Environ.* 163 (2015) 547–553.
- [18] Y. Huang, H. Li, M.-S. Balogun, W. Liu, Y. Tong, X. Lu, H. Ji, *ACS Appl. Mater. Interfaces* 6 (2014) 22920–22927.
- [19] Y. Huang, H. Li, W. Fan, F. Zhao, W. Qiu, H.-B. Ji, Y. Tong, *ACS Appl. Mater. Interfaces* 8 (2016) 27859–27867.
- [20] Y. Huang, B. Long, H. Li, M.S. Balogun, Z. Rui, Y. Tong, H. Ji, *Adv. Mater. Interfaces* 2 (2015) 1500249.
- [21] Y. Wang, K. Deng, L. Zhang, *J. Phys. Chem. C* 115 (2011) 14300–14308.
- [22] J. Di, J. Xia, S. Yin, H. Xu, L. Xu, Y. Xu, M. He, H. Li, *J. Mater. Chem. A* 2 (2014) 5340–5351.
- [23] L. Ye, K. Deng, F. Xu, L. Tian, T. Peng, L. Zan, *Phys. Chem. Chem. Phys.* 14 (2012) 82–85.
- [24] W. Fan, H. Li, F. Zhao, X. Xiao, Y. Huang, H. Ji, Y. Tong, *Chem. Commun.* 52 (2016) 5316–5319.
- [25] Y. Yang, C. Wang, J. Hou, J. Dai, *Mater. Lett.* 57 (2003) 2185–2188.
- [26] H.G. Yang, C.H. Sun, S.Z. Qiao, J. Zou, G. Liu, S.C. Smith, H.M. Cheng, G.Q. Lu, *Nature* 453 (2008) 638–641.
- [27] X. Chen, L. Liu, P.Y. Yu, S.S. Mao, *Science* 331 (2011) 746–750.
- [28] R. Schaub, E. Wahlström, A. Rønnau, E. Lagsgaard, I. Stensgaard, F. Besenbacher, *Science* 299 (2003) 377–379.
- [29] Z. Ning, X. Li, H. Ye, S. Chen, H. Ju, D. Liu, L. Yue, Y. Wei, C. Wang, X. Qian, *J. Am. Chem. Soc.* 138 (2016) 8928–8935.
- [30] H. Xu, P. Reunchan, S. Ouyang, H. Tong, N. Umezawa, T. Kako, J. Ye, *Chem. Mater.* 25 (2013) 405–411.
- [31] L. Pan, S. Wang, W. Mi, J. Song, J.J. Zou, L. Wang, X. Zhang, *Nano Energy* 9 (2014) 71–79.
- [32] J. Bao, X. Zhang, B. Fan, J. Zhang, M. Zhou, W. Yang, X. Hu, H. Wang, B. Pan, Y. Xie, *Angew. Chem. Int. Edit.* 127 (2015) 7507–7512.
- [33] Z. Dai, F. Qin, H. Zhao, J. Ding, Y. Liu, R. Chen, *ACS Catal.* 65 (2016) 892–898.
- [34] D. Jiang, W. Wang, L. Zhang, Y. Zheng, Z. Wang, *ACS Catal.* 5 (2015) 4851–4858.
- [35] Y. Huang, W. Fan, B. Long, H. Li, W. Qiu, F. Zhao, Y. Tong, H. Ji, *J. Mater. Chem. A* 4 (2016) 3648–3654.
- [36] Y. Huang, K. Ye, H. Li, W. Fan, F. Zhao, Y. Zhang, H. Ji, *Nano Res.* (2016) 1–12.
- [37] J. Yang, D. Li, Z. Zhang, Q. Li, H. Wang, *J. Photochem. Photobiol. A: Chem.* 137 (2000) 197–202.
- [38] L. Li, J. Ya, F. Hu, Z. Liu, L. E, *J. Energy Chem.* 25 (2016) 740–746.
- [39] Y. Zheng, W. Wang, D. Jiang, L. Zhang, *J. Chem Eng.* (2016) 21–27.
- [40] Y. Huang, B. Long, M. Tang, Z. Rui, M.-S. Balogun, Y. Tong, H. Ji, *Appl. Catal. B Environ.* 181 (2016) 779–787.
- [41] S. Weon, W. Choi, *Environ. Sci. Technol.* 50 (2016) 2556–2563.
- [42] G. Liu, T. Wang, S. Ouyang, L. Liu, H. Jiang, Q. Yu, T. Kako, J. Ye, *J. Mater. Chem. A* 3 (2015) 8123–8132.
- [43] F. Lei, Y. Sun, K. Liu, S. Gao, L. Liang, B. Pan, Y. Xie, *J. Am. Chem. Soc.* 136 (2014) 6826–6829.
- [44] H. Huang, K. Xiao, Y. He, T. Zhang, F. Dong, X. Du, Y. Zhang, *Appl. Catal. B Environ.* 199 (2016) 75–86.
- [45] P. Jian, L. Gang, G.Q. Lu, H.M. Cheng, *Angew. Chem. Int. Ed.* 50 (2011) 2133–2137.
- [46] K.H. Ye, Z. Chai, J. Gu, X. Yu, C. Zhao, Y. Zhang, W. Mai, *Nano Energy* 18 (2015) 222–231.
- [47] W. Yang, L. Zhang, J. Xie, X. Zhang, Q. Liu, T. Yao, S. Wei, Q. Zhang, Y. Xie, *Angew. Chem. Int. Ed.* 55 (2016) 6828–6832.